This figure "fig1-1.gif" is available in "gif" format from:

This figure "fig6-1.gif" is available in "gif" format from:

This figure "fig1-2.gif" is available in "gif" format from:

This figure "fig2.gif" is available in "gif" format from:

This figure "fig6-2.gif" is available in "gif" format from:

This figure "fig1-3.gif" is available in "gif" format from:

This figure "fig3.gif" is available in "gif" format from:

This figure "fig6-3.gif" is available in "gif" format from:

This figure "fig1-4.gif" is available in "gif" format from:

This figure "fig4.gif" is available in "gif" format from:

This figure "fig1-5.gif" is available in "gif" format from:

This figure "fig5.gif" is available in "gif" format from:

This figure "fig1-6.gif" is available in "gif" format from:

This figure "fig6.gif" is available in "gif" format from:

This figure "fig1-7.gif" is available in "gif" format from:

This figure "fig7.gif" is available in "gif" format from:

This figure "fig1-8.gif" is available in "gif" format from:

This figure "fig8.gif" is available in "gif" format from:

This figure "fig1-9.gif" is available in "gif" format from:

This figure "fig9.gif" is available in "gif" format from:

This figure "fig1-10.gif" is available in "gif" format from:

This figure "fig10.gif" is available in "gif" format from:

This figure "fig1-11.gif" is available in "gif" format from:

This figure "fig11.gif" is available in "gif" format from:

This figure "fig1-12.gif" is available in "gif" format from:

This figure "fig12.gif" is available in "gif" format from:

This figure "fig1-13.gif" is available in "gif" format from:

This figure "fig1-14.gif" is available in "gif" format from:

This figure "fig1-15.gif" is available in "gif" format from:

This figure "fig1-16.gif" is available in "gif" format from:

This figure "fig1-17.gif" is available in "gif" format from:

This figure "fig1-18.gif" is available in "gif" format from:

This figure "fig1-19.gif" is available in "gif" format from:

This figure "fig1-20.gif" is available in "gif" format from:

This figure "fig1-21.gif" is available in "gif" format from:

This figure "fig1-22.gif" is available in "gif" format from:

This figure "fig1-23.gif" is available in "gif" format from:

http://arXiv.org/ps/astro-ph/0105515v1

This figure "fig1-24.gif" is available in "gif" format from:

http://arXiv.org/ps/astro-ph/0105515v1

A SURVEY FOR INFALL MOTIONS TOWARD STARLESS CORES. II. CS(2-1) AND $N_2H^+(1-0)$ MAPPING OBSERVATIONS¹

Chang Won Lee^{1,2}, Philip C. Myers¹, & Mario Tafalla^{1,3}

¹Harvard-Smithsonian Center for Astrophysics, 60 Garden Street, MS 42, Cambridge, MA 02138, USA

²Taeduk Radio Astronomy Observatory, Korea Astronomy Observatory, 36-1 Hwaam-dong, Yusung-gu, Taejon 305-348, Korea

³Observatorio Astronómico Nacional, Alfonso XII, 3, E-28014 Madrid, Spain E-mail: cwlee@cfa.harvard.edu, pmyers@cfa.harvard.edu, tafalla@oan.es

ABSTRACT

We present the results of an extensive mapping survey of 'starless' cores in the optically thick line of CS(2-1) and the optically thin lines of N_2H^+ (1 – 0) and $C^{18}O$ (1 – 0). The purpose of this survey was to search for signatures of extended inward motions. A total of 53 targets were observed in the three lines with the FCRAO 14m telescope. Thirty three regions were mapped in both CS and N_2H^+ , and thirty seven well-defined N_2H^+ cores have been identified. The N_2H^+ emission is generally compact enough to find a peak, while the CS and $C^{18}O$ emissions are more diffuse. For each core, we have derived the normalized velocity difference (δV_{CS}) between the thick CS and thin N_2H^+ peak velocities. We define 10 'strong' and 9 'probable' infall candidates, based on δV_{CS} analysis and on the spectral shapes of CS lines.

From our analysis of the blue-skewed CS spectra and the δV_{CS} parameter, we find typical infall radii of 0.06-0.14 pc. Also, using a simple two layer radiative transfer model to fit the profiles, we derive one-dimensional infall speeds, half of whose values lie in the range of 0.05-0.09 km s⁻¹. These values are similar to those found in L1544 by Tafalla et al., and this result confirms that infall speeds in starless cores are generally faster than expected from ambipolar diffusion in a strongly sub-critical core. In addition, the observed infall regions are too extended to be consistent with the

¹To appear in Astrophysical Journal Supplement Series

'inside-out' collapse model applied to a very low-mass star. In the largest cores, the spatial extent of the CS spectra with infall asymmetry is larger than the extent of the N_2H^+ core by a factor of 2-3. All these results suggest that extended inward motions are a common feature in starless cores, and that they could represent a necessary stage in the condensation of a star-forming dense core.

Subject headings: ISM: Globules; ISM: Kinematics and Dynamics; Stars: Formation

1 INTRODUCTION 3

1. Introduction

Inward gas motions are a key element of star formation. Ambipolar diffusion or dissipation of turbulence can drive such motions during the process of core formation (e.g., Shu et al. 1987, Ciolek & Mouschovias 1995, Nakano 1998, Myers & Lazarian 1998), and gravitational collapse is the basis of any model of stellar birth (e.g., Shu 1977). Despite the theoretical expectation for a prevalence of inward motions in star-forming regions, little observational evidence for this type of kinematics still exists. Only during the last decade, with its rapid development of mm-radio telescope instrumentation, have the first infall candidates emerged (Zhou et al. 1993), and systematic work on infall motions has been possible (Mardones et al. 1997, Gregersen et al. 1997).

Inward motions are inferred by observing the "infall asymmetry" in spectral lines: a combination of a double peak with a brighter blue component or a skewed single blue peak in an optically thick spectrum, and a Gaussian single peak in an optically thin line (Leung & Brown 1977, Zhou 1995, Myers et al. 1996). As target sources, starless dense cores –regions which do not yet contain young stellar objects (YSOs)— are excellent candidates, as they are expected to display inward motions in the earliest stage of the star-forming process, and therefore suffer from the least contamination by bipolar outflows. The recent observations of the starless core L1544 by Tafalla et al. (1998, hereafter T98) and Williams et al. (1999) show that the infall asymmetry is spatially too extended ($\sim 0.1 \text{ pc}$) to be consistent with the 'inside-out' collapse model of Shu (1997), and that the large inward speed (up to 0.1 km s⁻¹) is also too fast to result from ambipolar diffusion in a strongly sub-critical core. This inconsistency of L1544 with the 'standard' models casts many questions on the physics of inward motions occurring in the very early stage of star formation: Are the extended inward motions a general phenomenon that all cores should experience to form the star? If so, what would be the typical infall parameters of the collapsing cores, e.g., the typical infall size, speed, and mass infall rate, which may help us infer basic physics associated with inward motions?

To answer the above questions, a detailed study of infall motions in starless cores is necessary. Lee, Myers, & Tafalla (1999) (hereafter LMT99) have carried out the first such work by studying 220 starless cores with single pointing observations in the optically thick and thin tracers CS(2-1) and N_2H^+ (1-0). These authors found that inward motions are statistically significant in starless cores. A similar study of HCO^+ (3-2) emission found frequent infall asymmetry in 17 starless cores having sub-millimeter continuum (Gregersen & Evans 2000). Single pointing observations, however, do not guarantee that each core with infall asymmetry is necessarily undergoing inward motions, because other kinematics such as differential rotation and bipolar outflow can mimic that feature (Adelson & Leung 1988, Zhou 1995). In order to clarify the real core kinematics, mapping surveys in both optically thick and thin spectral lines are therefore necessary.

The goal of this paper is to complement the results of LMT99 with an extensive mapping survey of dense starless cores in optically thick CS (2–1) and thin $N_2H^+(1-0)$ [and $C^{18}O(1-0)$] lines, so we can address the questions suggested by the L1544 study. This paper is structured

2 OBSERVATIONS 4

as follows: in §2 we explain details of the observations such as target selection, observational equipment and methods, and data reduction. Detection statistics, mapping results, quantitative analysis of the infall size, speed, mass infall rate, and interesting individual cores are described, and implications of the observational results are discussed in §3. In the last section we summarize the main conclusions of this work.

2. Observations

Our mapping survey was carried out in CS(2-1), N_2H^+ (1-0), and $C^{18}O$ (1-0) with the 14m telescope of the Five College Radio Astronomy Observatory (FCRAO)¹. Targets were selected according to different criteria (see last column of Table 1). Thirty-four targets were selected based on the single-pointing observations of LMT99. We observed 7 strong and 9 probable infall candidates defined by LMT99, as well as 18 targets showing strong CS and N_2H^+ emission from LMT99. Twelve targets were selected from their NH₃ detection by Benson & Myers (1989, hereafter BM89), and seven targets are from Lee & Myers (1999, hereafter LM99). Overall, the starless cores in our target list are nearby (within a few hundred pc), have high extinction $(A_v \sim 5^m$ based on the original Lynds selection, Lynds 1962), have optical sizes of $0.05 \sim 0.35$ pc (LM99), and typical line widths (FWHM of N_2H^+) of 0.2 - 0.4 km s⁻¹ (Fig. 2 of this study).

In a quantitative study of infall motions using narrow line profiles, like this one, it is important to use accurate frequencies for the different molecular lines (see LMT99). Recent laboratory measurements (Gottlieb 2000, private communication) have improved the precision of the frequency estimates for CS(2-1) (97980.953±0.002 MHz) and $C^{18}O$ (1-0) (109782.173±0.002 MHz), and in the rest of this paper we will use these new values. To obtain an equally accurate frequency for the N_2H^+ (1-0) "isolated" ($F_1F = 01 - 12$) component, we have used new astronomical measurements of the extremely narrow lines toward L1512, where taking as reference the above value of the $C^{18}O$ (1-0) frequency, we have derived an N_2H^+ (1-0) frequency of 93176.258 MHz (see appendix). This new frequency set reduces the velocity shift between CS and N_2H^+ in the LMT99 study by about 0.013 km s⁻¹. The effect of this change in the LMT99 conclusions is small, and is discussed in detail in the appendix.

Our extensive observations were made possible with the focal plane receiver arrays QUARRY and SEQUOIA at FCRAO. At the beginning of our survey (1997 January), the QUARRY system having 15 elements was used for a quick survey of about 42 targets in CS(2–1), N₂H⁺(1–0), and C¹⁸O(1–0). After that season, the new single sideband 16 element focal plane array receiver SEQUOIA became available, and observations with this instrument were performed during 1998 March, April, and December, 1999 February and November, and 2000 January. The system

¹FCRAO is supported in part by the National Science Foundation under grant AST 94-20159, and is operated with permission of the Metropolitan District Commission, Commonwealth of Massachusetts

temperature was typically around 300 - 400 K for QUARRY and 140 - 180 K for the SEQUOIA, so most high quality data have been obtained with the SEQUOIA. Thus, if data from both receivers are available, only the SEQUOIA data are presented. QUARRY has been designed to make a beam-sampled map of $200'' \times 250''$ in a 50'' grid with two pointings (which is called one footprint map) while SEQUOIA was used to make a beam-sampled map of $352'' \times 352''$ in a 44'' grid with four pointings (which is one footprint map). The telescope beam size (FWHM) is approximately 52'' at the CS(2-1) and $N_2H^+(1-0)$ frequencies, and the main beam efficiency at these frequencies is about 0.56.

As back-ends, we used autocorrelation spectrometers with spectral channels of 10 and 20 KHz, achieving velocity resolutions of around 0.03 - 0.06 km s⁻¹. Such high resolutions are necessary for discerning the small amount of velocity shift between the optically thick and thin spectra. All observations were performed in frequency switching mode with a 4 MHz offset for CS, and a 8 MHz offset for N₂H⁺ and C¹⁸O. The telescope pointing was checked and corrected using 86 GHz SiO maser sources whenever the observing region was changed, and its accuracy was better than 10". The telescope focus was optimized prior to each pointing check. In the QUARRY observation, all sources were observed in just one footprint mode, and many extended sources were not fully covered. During the SEQUOIA observations, we made several footprint maps to cover the whole area of each core. Most of the spectral line data reduction was performed using the 'CLASS' reduction software (Buisson et al. 1994).

3. Results and Discussion

3.1. Detection Statistics

Details of our observations of a total of 53 targets are summarized in Table 1. Fifty out of 52 sources were detected in CS(2-1), 34 out of 45 were detected in CS(2-1), and 28 out of 29 were detected in CS(2-1) and CS(2-1) and CS(2-1) and CS(2-1) lines. It should be noted that some sources consist of several smaller cores, while some sources were not fully mapped and their spatial extent is unknown. Therefore, the number of fully mapped cores is different from the number of observed or detected sources, and the central positions of the cores are sometimes different from the centers of the maps. We identify thirty-seven CS(2-1) the spatial extent and the strongest positions are well defined, and we list the coordinates, map sizes, velocities, line widths, and other information of these cores in Table 2.

3.2. Gas Distribution and Spectra

We present a summary of our data in Fig. 1, where we preferentially show sources with well defined N_2H^+ (1 – 0) distribution and interesting CS profiles. For space reasons, we do not present sources for which N_2H^+ (1 – 0) was not observed, not detected, or partly mapped, and where the CS profiles are noisy and show no asymmetric features. We have excluded L1445, for which N_2H^+ is not detected although its CS spectra show a self absorption feature while $C^{18}O$ does not. The combination of CS and $C^{18}O$ spectra in this source suggests the presence of infall asymmetry, as in LMT99. We specially include N_2H^+ maps for L1495 and L1155C (Fig. 1-4 & Fig. 1-20) to illustrate their multiple cores with extended N_2H^+ distribution.

Most of the data are presented with a CS profile map superposed onto the N_2H^+ integrated intensity distribution on the left panel and with the averaged CS and N_2H^+ spectra over the half maximum contour in the N_2H^+ intensity map on the right panel. The dashed lines on the profiles are the systemic velocities derived from Gaussian fits to the N_2H^+ data using the relative frequencies and intensities of the 7 hyperfine components determined by Caselli et al. (1995).

As described in LMT99, there is a general trend of double peaks and asymmetric features in the CS spectra, while most of the N_2H^+ and $C^{18}O$ lines have a single peak and an almost Gaussian shape. Column 11 of Table 2 gives our estimates of the optical depth of the isolated $(F_1F = 01 - 12)$ hyperfine component, $\langle \tau_{N_2H^+} \rangle$, defined as one-ninth of the total optical depth of the 1-0 spectrum. This is determined by using the hyperfine structure (hfs) fitting routine in CLASS (Buisson et al. 1994), averaged over all spectra having S/N > 5 in a map. We note that the optical depth of the isolated N_2H^+ component for most cores is lower than 1.0, indicating that this component is optically thin.

To compare the spectra of the two thin tracers, N_2H^+ and $C^{18}O$, we make averages of the spectra with S/N > 5 for ten sources observed with QUARRY ($C^{18}O$ observations were conducted with QUARRY only). In this way we find that the shapes of both lines are similar (Gaussian), while the $C^{18}O$ line width (FWHM) is always larger than that of N_2H^+ by around 0.1-0.4 km s⁻¹. The difference between the line velocities of the two tracers is fairly small (mean± standard deviation = 0.007 ± 0.078 km s⁻¹).

Spatially, the N_2H^+ emission is usually compact enough to define a core peak, while the CS and $C^{18}O$ emissions are much more diffuse. The greater extent of the CS and $C^{18}O$ emissions could be due to their lower effective critical density compared to that of N_2H^+ , while the lower concentration of CS and $C^{18}O$ toward the core peak may be due to depletion of these molecules or self-absorption in the case of CS, while N_2H^+ experiences little depletion (e.g., Aikawa et al. 2001, Tafalla et al. 2001, in preparation) or self-absorption. This greater extension of CS and $C^{18}O$ compared to N_2H^+ is similar to the pattern seen when comparing CS, $C^{18}O$, and NH_3 maps in low-mass cores with and without YSOs (Myers et al. 1991)

Using the core size values presented in Table 2 (expressed as an equivalent radius $(A/\pi)^{1/2}$,

where A is area inside the N_2H^+ half maximum contour), we compare in Fig. 2 core sizes and line widths for the N_2H^+ emission. The figure shows a slight indication of a line width-size relation, which is similar to, but not as significant as, that in Fig. 6 of Jijina, Myers & Adams (1999) using NH₃ cores without IRAS sources. As seen in the figure, the typical sizes of the N_2H^+ cores are between ~ 0.05 pc and ~ 0.13 pc, and the typical line widths of the cores are 0.2-0.4 km s⁻¹.

3.3. Distribution of the Velocity Difference δV_{CS} Between the Optically Thick CS and the Thin N_2H^+ Spectra

The normalized velocity difference between an optically thick and a thin line (δV) has been found to be a sensitive measure of relative line shifts indicative of inward motions (e.g., Mardones et al. 1997, LMT99). For this work, we use the CS(2–1) and N₂H⁺(1–0) lines as thick and thin tracers, respectively, and define $\delta V_{CS} = (V_{CS} - V_{N_2H^+})/\Delta V_{N_2H^+}$. For each spectrum in our 35 starless cores, we measure the velocity of the peak CS intensity (V_{CS}) from a Gaussian fit to the brightest spectral component after masking the less bright component or the skewed part, and measure the N₂H⁺(1–0) velocity ($V_{N_2H^+}$) from a hyperfine Gaussian fit to its seven components using the CLASS software. The FWHM of the N₂H⁺ emission ($\Delta V_{N_2H^+}$) is also derived from the hyperfine fit. To avoid ambiguity when choosing the bright CS component, we follow LMT99 and omit those CS spectra for which a Gaussian fit indicates a difference between the blue and red components smaller than the 1 σ noise of the spectrum.

Table 2 presents our estimates of δV_{CS} for each core, together with estimates of the CS and N_2H^+ velocities derived using spectra with peak S/N larger than 5. Note that the CS and N_2H^+ velocities, and the N_2H^+ line widths are averages over the core (\pm standard error of the mean, or s.e.m): $\langle V_{CS} \rangle = \sum_i V_{CS}^i/N$, $\langle V_{N_2H^+} \rangle = \sum_i V_{N_2H^+}^i/N$, and $\langle \Delta V_{N_2H^+} \rangle = \sum_i \Delta V_{N_2H^+}^i/N$, where N is the number of spectra with peak S/N larger than 5. The parameter $\langle \delta V_{CS} \rangle$ ($= \sum_i \delta V_{CS}/N$) presented in the last column is the average (\pm s.e.m) of all δV_{CS} s obtained in each core considering the CS and N_2H^+ spectra whose peak S/N is better than 5. The number N of δV_{CS} values and the radius R of the spatial extent of the region having spectra with peak S/N better than 5 are given in columns 8 and 9. R was estimated as half of the largest distance between core positions for which δV_{CS} s can be derived using spectra with S/N greater than 5. We have also estimated δV_{CS} for the average CS and N_2H^+ spectra, but this parameter is not significantly different from $\langle \delta V_{CS} \rangle$ for most sources. Thus, its use instead of $\langle \delta V_{CS} \rangle$ would not affect our conclusions.

The value of $\langle \delta V_{CS} \rangle$ in each core is a useful indicator of the global overabundance of blue or red spectra, and suggests a dominance of inward or outward motions. Fig. 3 plots the distribution of $\langle \delta V_{CS} \rangle$ for our sample, showing that most of our sources have a global overabundance of blue spectra characteristic of inward motions. The excess of sources with overabundance of blue spectra in our sample, however, does not necessarily reflect the statistical infall excess in starless cores found in the previous single pointing survey (LMT99), because many sources in our present

sample have been selected with a bias toward infall candidates from previous observations. What the results in Fig. 3 do show is that most infall candidates from the previous single pointing observations are now confirmed as infall candidates when full maps are made, so the infall classification in LMT99 does not arise from the observation of an special position, but from a real property of the core as a whole.

3.4. δV_{CS} Related Parameters and Classification of Starless Cores

Here we introduce two δV_{CS} related parameters in order to further measure the distribution of asymmetric profiles in a core and to classify cores in relation to inward motions. One parameter is the blue excess $E = (N_- - N_+)/N$, where N_- is the number of positions with $\delta V_{CS} \leq -5 \sigma_{\delta V_{CS}}$, N_+ is the number of positions with $\delta V_{CS} \geq 5 \sigma_{\delta V_{CS}}$, N_+ is the number of positions with $\delta V_{CS} \geq 5 \sigma_{\delta V_{CS}}$, N_+ is the total number of positions for which δV_{CS} was determined, and $\sigma_{\delta V_{CS}}$ is a propagation error of δV_{CS} . We have chosen n=5 in n $\sigma_{\delta V_{CS}}$ for the limit value to represent the degree of significance of the skewness in the CS profile with respect to N_2H^+ line. This is a compromise between those which give too much noise (lower n) and too few cases to allow analysis (higher n). While n=5 is arbitrarily chosen, our results are not sensitive to the exact choice of n for n=4 to 6.

The other parameter we introduce is a P value of a student t-test for the δV_{CS} distribution for each core, which is the probability of drawing our δV_{CS} distribution from a zero mean t-distribution. This P value is useful to measure the statistical significance of the dominance of the blue or red asymmetry in the cores. A value very close to zero means that the distribution of the observed δV_{CS} is very far from the symmetric zero mean t-distribution. The E and P values for each core are listed in the last columns of Table 3.

As Figures 4 and 5 illustrate, the E and P parameters have a very close correlation with $<\delta V_{CS}>$. Fig. 4 indicates that the blue excess increases as $<\delta V_{CS}>$ becomes more negative, and Fig. 5 shows that P approaches zero as $<\delta V_{CS}>$ deviates from zero (i.e., as a global overabundance of blue or red asymmetry gets more significant). Combining these E and P parameters with additional spectral properties, we now proceed to classify starless cores. First, cores can be classified in two main groups: cores with "significant excess (SE)" and cores with "no significant excess (NSE)". Then, the "SE" cores would be divided into cores with "significant blue excess" which would be further subdivided into those with double CS peaks and those with just single CS peak, and cores with "significant red excess". The "NSE" cores might be subdivided into a group where the spread in δV_{CS} is significantly positive or negative, and into a group where the spread in δV_{CS} is large, and there are several points with significantly blue or red δV_{CS} .

In Fig. 6 we display the number distributions of δV_{CS} for all cores according to the above classification, excluding cores with a small number of δV_{CS} measurements (< 7), for which the parameters are not statistically significant, and cores with noisy detection for which the number

of positions with measurements of S/N > 5 is less than 3. We now describe in more detail each of the groups.

Group 1 corresponds to cores with "very significant blue excess" and double CS peaks near the peak intensity position of N_2H^+ . These cores have high blue excess ($E \gtrsim 0.35$) and low P ($\lesssim 0.1$), or significantly skewed δV_{CS} distribution to the blue (Fig. 6-a), corresponding to objects with overwhelming overabundance of blue asymmetric CS spectra. Note that these criteria classify the well known infall candidate L1544 as a member of group 1, and we will refer to the sources in this group as 'strong infall candidates'. This group consists of L1498, L1495A–S, L1544 L1689B, L234E-S, L492, L694-2, L1155C-2, and L1155C-1, and possibly L183, as discussed below.

Group 2 contains sources with "significant blue excess" and *single*-peaked CS spectra, which are blue-skewed, near the peak intensity position of N_2H^+ . These cores have fairly high blue excess $(E \gtrsim 0.1)$ and low P $(\lesssim 0.1)$. This group corresponds to 'probable infall candidates' (Fig. 6-b), and consists of L1355, TMC2, TMC1, L1552, L1622A-2, L158, and L234E-C, possibly L981 and L1197, as discussed below.

Group 3 contains sources with "significant red excess" having high red excess (E \leq -0.15) and δV_{CS} distributions significantly asymmetric toward the red (P \approx 0.0) (Fig. 6-c), but no blue asymmetry in the CS spectra (N₋ = 0). Three sources belong to this group: L1521F, L429-1, and CB246.

Group 4 corresponds to cores with "no significant excess" having small spread in δV_{CS} . The sources in this group have little blue or red excess ($E \approx 0$), and have δV_{CS} distributions with rather small rms (one standard deviation ≤ 0.3) (Fig. 6-d). Sources in this category are L1333, L1495B, L1400A, L1517B, L1622A-1, L1696A, and L234E-N.

Finally, group 5 contains cores with "no significant excess" and a large spread in δV_{CS} . These sources show little excess (E \approx 0) either because they contain a similar number of spectra of significantly blue or red δV_{CS} , or because they have few spectra of significantly blue or red δV_{CS} . In any case, the distribution of δV_{CS} has a larger rms than that of group 4 (one standard deviation $\gtrsim 0.4$) (Fig. 6-e). Sources in this group are L1495A–N, L1507A, and L1512.

Although the above criteria seem to classify well the cores, it is possible that they still miss some infall candidates. L183, for example, has the largest angular area mapped in both CS and N_2H^+ , and has a different pattern of profiles depending on the region considered (Fig. 1-13). Within the half maximum contour of N_2H^+ , L183 shows extended infall asymmetry, and the statistics of its spectra are characteristic of a strong infall candidate (E=0.6 and P=0.00). Toward the outer part of the core, however, we find profiles with red asymmetry (S-W of the core), skewed infall asymmetry, and symmetric lines, and when all the spectra are considered we obtain E=0.12 and P=0.62, which will not classify the core as an infall candidate. This different behavior of the inner and outer regions is what one would expect if the inner core has inward motions while the outer layers are static. For this reason, we classify **L183** as a strong infall candidate.

Other sources which may have a pattern similar to L183 and present infall asymmetric profiles toward the inner core and symmetric profiles outside are L1689B and L234E-S. Unfortunately, the outer spectra in these sources are rather weak, and the infall pattern hard to discern. These sources deserve a more detailed study of their spectral properties.

As mentioned before, we have not included in our classification sources with a small number of δV_{CS} measurements (< 7) and sources with noisy detections. Sources excluded in this way are CB23, L134A, L981-1, L1063, and L1197. Note that **L981-1** and **L1197** show typical infall profiles in their compact N₂H⁺ cores, so they are likely to be considered probable infall candidates when more sensitive observations are carried out.

3.5. Infall Candidates from Mapping Observations and from Single Pointing Observations

In our survey we have mapped 15 infall candidates suggested by LMT99. We now check whether these infall candidates from single-pointing observations continue being infall candidates after a complete mapping observation.

According to the above core classification, 11 of the 15 LMT99 sources are now classified as strong or probable infall candidates. These sources are L1355, L1498, L183, L158, L694-2, L1155C-1, TMC2, L1622A-2, L1689B, L234E-S, and L492 (the source name L234E-1 used in the previous single pointing observations has been changed to L234E-S in this survey).

L1521F was considered a strong infall candidate in LMT99 because of its blue asymmetry in the CS profile, but in our mapping survey it shows a reverse asymmetry – red asymmetry – which is also extended. As the Haystack telescope beam used in LMT99 is about one half of the FCRAO beam, the infall asymmetry in the smaller beam and the red asymmetry in the larger beam suggest that in this core the direction of the gas motions may change toward the center. More observations are needed to understand this change.

CB23 was classified as a probable infall candidate by LMT99, and our mapping survey finds a slight asymmetric CS profile at the center. However, all other profiles have a Gaussian shape, making the E value of this source equal to zero. The small number of δV_{CS} measurements in this core (4) leaves it unclassified.

Another source which remains unclassified in this study, despite being a probable infall candidate in LMT99 is L1445, as it was not detected in N_2H^+ by our FCRAO observations. The LMT99 infall candidates L1524-4 and B18-3 have not been mapped with the FCRAO telescope, so their infall status cannot be tested. Finally, new infall candidates not considered as such by LMT99 include TMC1, L1552, and L1155C-2, and all show extended infall asymmetry in their profile maps.

In summary, most infall candidates from the single pointing observations remain bona fide

candidates, although a minority of sources show spectral profiles different from those inferred using the single pointing data.

3.6. Infall Radius, Speed, and Mass Infall Rate of Starless Infall Candidates

We now estimate the infall radius, speed, and mass infall rate for our infall candidates in groups 1 and 2, as well as for L183, L981-1, and L1197. We consider two cases depending on the choice of spectra used to calculate the infall parameters. Case 1 is called the 'weak' case (indicated by 'W'), and considers all blue asymmetric spectra satisfying $\delta V_{CS} \leq -5 \sigma_{\delta V_{CS}}$. Case 2 is referred as the 'strong' case (indicated by 'S'), and considers only the CS spectra with double-peaked infall asymmetry satisfying $\delta V_{CS} \leq -5 \sigma_{\delta V_{CS}}$.

3.6.1. Infall Radius

We estimate the infall radius of each core from the spatial distribution of δV_{CS} by measuring the regions where δV_{CS} is significantly negative. We define the infall radius as one half the largest distance between positions showing infall asymmetry of $\delta V_{CS} \leq -5 \ \sigma_{\delta V_{CS}}$ in their spectral profiles. For L158, L234E-C, and L1197, which have only one position with $\delta V_{CS} \leq -5 \ \sigma_{\delta V_{CS}}$, we take as infall radius one half the linear size of the telescope beam FWHM ($\sim 26''$). Table 4 gives our estimates of the infall radii of the cores for the 'weak' and 'strong' cases.

Our method of deriving infall radii from the δV_{CS} distribution is limited by the spatial extent of the N_2H^+ emission. In some cores (e.g., L1689B and L158), the region with blue-skewed CS spectra is more extended than the region with detected N_2H^+ , so a method based on the δV_{CS} distribution gives infall radii smaller than one based on the spatial extent of the blue-skewed CS profiles. Thus, as an alternative, we also measure infall radii by using the spatial extent of the blue-skewed CS profiles, taking as infall radius one half the largest separation between positions with skewed CS spectra.

We present the estimated infall radii for all three cases in Table 4, and show their number distribution in Fig. 7. The statistics show that infall radii are typically about 0.06-0.10 pc for the 'weak' and 'strong' δV_{CS} cases, and around 0.06-0.14 pc for the estimates based on the extent of the blue-skewed CS profiles.

3.6.2. Infall Speed

We estimate infall speeds of the 'weak' and 'strong' cases for our infall candidates by applying a simple two layer model similar to that of Myers et al. (1996). For this, we average all blue asymmetric spectra satisfying the 'weak' and 'strong' cases, respectively.

Our two-layer model consists of a cool (2.7 K) absorbing front screen moving away from us and a warm emitting rear layer approaching us with same speed. The emerging brightness distribution in terms of the line brightness temperature ΔT_B is given by (see Myers et al. 1996):

$$\Delta T_B = J(T_r)(1 - e^{-\tau_r})e^{-\tau_f} + J(T_b)(e^{-\tau_f - \tau_r} - e^{-\tau_f}),$$

where $J(T) = T_0/[exp(T_0/T) - 1]$, $T_0 = h\nu/k$, ν is the frequency, h is Planck's constant, k is Boltzmann's constant, T_b is the cosmic background temperature (2.7 K), T_r is the excitation temperature of the rear layer, and τ_f and τ_r are the optical depths of the front and rear layers, respectively. The optical depths are given by $\tau_f = \tau_0 \exp[-(v - V_f)^2/2\sigma^2]$, and $\tau_r = \tau_0 \exp[-(v + V_r)^2/2\sigma^2]$, where τ_0 is the peak optical depth, V_f and V_r are the systemic velocities of the front and the rear layers, respectively, and σ is the velocity dispersion of the gas in both layers.

Given the above equation, our fitting procedure has 5 free parameters $[\tau_0, V_f = V_r (= V_{in,z}/2), T_r, \sigma \ (= \Delta V_{FWHM}/2.355)$, and $V_{LSR}]$. Usually, σ and V_{LSR} are very well constrained by the width and centroid velocity of the observed spectra. The rest of the free parameters depend on different features of the line profile. The peak optical depth τ_0 is sensitive to the depth of the self-absorption dip, the infall speed $V_{in,z}$ primarily affects the ratio of blue to red peaks of a self-absorbed spectrum, and the excitation temperature of the rear layer T_r controls the overall intensity scale of the spectrum. As these parameters affect different aspects of the line profile, they are usually well constrained, and tests repeating the fitting procedure return very similar values of these parameters.

The results of our modeling are presented in Fig. 8, where model spectra (thick solid lines) are shown superposed to the observed spectra (thin solid histograms). For space reasons, we show results of the weak case for the cores without strong case, and of the strong case only for cores with both cases. (L694-2 is the exception). Note that spectra for the two cases are only slightly different, and as it can be seen, the fit is quite good in most cases. The numerical results of the non-linear least squares fitting procedure are listed in Table 4.

The most important parameter derived from our model fitting is $V_{\rm in,z}$, so we have estimated its uncertainty with a semi-empirical procedure. We have taken a best-fit spectrum for L694-2 (strong case), added random noise with the same rms as the observed noise, and made a new fit. By repeating this procedure 100 times, we have derived a 1 sigma uncertainty 0.001 km s⁻¹, which is much smaller than the estimated $V_{\rm in,z}$ (0.086 km s⁻¹). Although the uncertainty may be slightly larger for cores where the fit is not as good as in L694-2 (e.g., L1155C-2), the above estimate suggests that our $V_{\rm in,z}$ values are not dominated by noise.

To summarize the $V_{in,z}$ estimates, we present in Fig. 9 a histogram of this parameter, showing that most infalling starless cores have $V_{in,z}$ of 0.05-0.09 km s⁻¹ for both the 'weak' and the 'strong' case. It should be noted, however, that the infall speed derived here is the line-of-sight velocity, which is smaller than the three dimensional (3-D) infall speed (V_{in}) by a likely factor of about 1-2. Comparing our estimates with those of LMT99, we find a reasonable

agreement, despite the fact that the LMT99 values were simply derived by taking half of the velocity dispersion of the N_2H^+ line obtained from a single pointing observation.

3.6.3. Mass Infall Rate

The mass infall rate determines how fast matter is condensing through the surface of the infall radius (R_{in}). We estimate this rate from $4\pi R_{in}^2 \rho V_{in}$, assuming that the core has uniform density ρ and is spherically infalling with a speed V_{in}. Our two-layer model does not constrain well the density of the gas causing the absorption dip or shoulder in the CS profiles, so we approximate it by ρ (= $15\sigma^2/4\pi GR_{in}$), which is the density of a core in virial equilibrium with radius (R_{in}) and velocity dispersion (σ) (see column 11 of Table 4). Here the velocity dispersion is derived from the two layer model fit. In this way, gas densities are between about 3.0×10^3 and 4.1×10^5 cm⁻³, with a typical value of a few 10^4 cm⁻³.

The resulting mass infall rates for the strong and weak cases are between a few $10^{-6} \sim 10^{-5} \ \mathrm{M}_{\odot} \ \mathrm{yr}^{-1}$. Individual estimates for each source are given in the last column of Table 5. All these estimates are derived using the projected infall speed $(V_{\mathrm{in,z}})$, so the true mass infall rates, derived from the 3-D infall speeds, will be probably larger by a factor of 1-2.

3.7. Infall Radius and Core Size

A comparison of the size of the infall region with the core size is presented in Fig. 10 as a plot of the infall radius versus the radius of the N_2H^+ emission (listed in the 4th column of Table 2). Three cases are presented in the figure according to the method used in deriving the infall radius: (a) weak case, (b) strong case, and (c) case using the extent of the blue-skewed CS profiles.

The errors for both radii are difficult to specify for each source. The uncertainty of distance would be a major cause for the errors, however, such uncertainty would equally change both radii in the same way and so the tendency shown in Fig. 10 would not be affected due to the uncertainty of distance. The uncertainties of both radii which we can approximately give are the values obtained from repeating measurements, which are typically small (about between 0.01 - 0.02 pc) compared with the estimates of the radii.

Dashed lines in the figure correspond to core sizes equal to infall sizes. As seen in the figure, in strong case (b) the data are along the dashed line, i.e., larger cores tend to have equivalently larger infall zones. This is because the infall size in the strong case is strongly limited with an extent of distribution of CS profiles with double peaks which is localized around the central region of the N_2H^+ core.

In (a) and (c) cases, however, the slope of the data is even steeper than that of the dashed line, i.e., large cores tend to have a factor of about 2-3 larger infalling zones than their extents,

implying that the core tends to have wider infalling region as the core is becoming bigger, or vice versa. This result suggests that infall motions that we are seeing are likely involved in the building-up of the dense core.

3.8. Possible Interpretation of Extended Inward Motions

Taking as a whole the results in Table 4, we can see that the main features of the inward motions in our infall candidates are very similar to those found in L1544 by T98 and Williams et al. (1999). This indicates that L1544 is not exceptional in having extended infall asymmetry, and we interpret this as a suggestion that the extended infall phenomenon may be a necessary stage in core evolution

To investigate the cause of the extended inward motions in starless cores we explore different alternatives. First, we believe that these motions do not represent directly the process of forming a star, but of building up a dense core. Our cores have been selected to be starless in the sense that there is no associated IRAS point source (LM99), and so far no other evidence for embedded stellar objects in these cores has been found. Instead, there are supporting clues that our targets are starless, as the fact that the spectral lines from all sources are very narrow (N_2H^+ FWHM of about 0.2 - 0.4 km s⁻¹), and the fact that no source shows wide wing components in its profiles suggestive of the presence of outflow motions. This lack of evidence for star formation makes the extended inward motions (at least 0.06 pc in radius) incompatible with the "inside-out" collapse model of Shu (1977), because the large infall sizes imply large times since collapse started, and require the presence of detectable YSOs at the core centers, something we can easily rule out.

Alternative mechanisms for producing extended inward motions involve the process of ambipolar diffusion, or the dissipation of turbulent motions. Infall speeds, however, are usually over $\sim 0.05~\rm km~s^{-1}$, which is too fast to result from ambipolar diffusion in a strongly sub-critical core (e.g., 'standard' B_{UB} model of Ciolek & Mouschovias 1995 predicting $\sim 0.02~\rm km~s^{-1}$ at 0.05 pc). Still, the possibility of ambipolar diffusion can not be ruled out. For example, recent models for super-critical cores are found to produce infall speeds closer to $\sim 0.1~\rm km~s^{-1}$ at 0.05 pc (e.g., Ciolek & Basu 2000), and models of slightly sub-critical cores predict inward speeds intermediate between those of strongly sub-critical ambipolar diffusion and of dynamical motions (Zweibel 1998; Indebetouw & Zweibel 2000). Furthermore, a spherical core model which includes the effects of dust grains on field-gas coupling predicts extended inward motions of $\sim 0.1~\rm km~s^{-1}$ (Li 1999).

Alternatively, turbulent dissipation models (e.g., Myers & Lazarian 1998, Myers & Zweibel 2001) also predict extended inward motions, substantially faster ($\sim 0.1 \text{ km s}^{-1}$) than those from ambipolar distribution of a strongly sub-critical core.

Thus, super-critical, slightly sub-critical ambipolar diffusion, or turbulent dissipation may explain the presence of the extended inward motions we find, although more detailed models are still needed to settle this problem.

3.9. Individual Sources

In this section we briefly describe the kinematical characteristics and interesting features of some sources. We especially focus on those sources for which high S/N data were obtained. Detailed descriptions on the infall structure of some infall candidates will be presented in a future study.

L1498 – Our integrated intensity map of N₂H⁺ for L1498 shows that it has a well-defined gas distribution elongated NW to SE with a position angle of about -50° (Fig. 1-3). This source is well studied by several authors (e.g., Lemme et al. 1995, Kuiper, Langer, & Velusamy 1996, Wolkovitch et al 1997, and Gregersen & Evans 2000). L1498 has been suggested to be a classic example of a pre-protosteller core that may be on the verge of rapid collapse to form a protostar from CCS, NH₃, C₃H₂, HC₇N, C¹⁸O, and ¹³CO observations (Kuiper, Langer, & Velusamy 1996). Lemme et al. (1995) have first found the extended distribution of CS (3-2) profiles with double peaks of the blue peak brighter than the red peak. They interpreted this might be either from absorption by a foreground low density cloud or from presence of two layers of gas with slightly different line-of-sight velocities, with a double peaked feature of the optically thin tracer, C³⁴S which was poorly detected. Our observation rules out the second possibility because the optically thin tracer N₂H⁺, detected with high S/N, shows clearly single peaked spectra, as seen in Fig. 1-3.

Infall asymmetry in the CS profiles is prominent and spatially extended. Interestingly, CS spectra of skewed single peak and double peaks are spatially mixed. The CS profile map shows infall profiles of double peaks near the peak N_2H^+ intensity and single skewed peak outside. Average profiles over the HM contour area of N_2H^+ intensity show typical infall asymmetry, suggesting that inward motions are globally dominant over the core. Such an indication is also seen in the distribution of δV_{CS} , which is overwhelmingly skewed to the blue (Fig. 6-a). This source is suggested to be a 'strong' infall candidate. Possible infall radius and speed are 0.05-0.08 pc and 0.03-0.08 km s⁻¹, and the derived mass infall rate is $0.09-0.13\times10^{-5}$ M_{\odot} yr⁻¹.

L1495– The N_2H^+ integrated intensity map in Fig. 1-4 shows that this core has three distinct N_2H^+ condensations: L1495A–N, S, and L1495–B. **L1495A**–N is elongated north-south (Fig. 1-5), and its extended infall asymmetry of CS profiles reverses to extended red asymmetry with respect to a NE–SW axis which crosses the center of the core (drawn with solid line in Fig. 1-5), suggesting the presence of differential rotation.

Fig 1-5 also shows the **L1495A** – **S** core, whose N_2H^+ emission is elongated approximately E-W. The CS spectra toward L1495A-S consistently show infall asymmetry, both in the form of skewed spectra and double-peaked profiles, like L1498. The infall radius inferred from the δV_{CS} distribution is about 0.09 pc, and the value from the skewed CS profiles is slightly larger (0.12 pc). The infall speed is estimated in 0.07 – 0.08 km s⁻¹, and the mass infall is $1.0-1.1\times10^{-5}~{\rm M}_{\odot}~{\rm yr}^{-1}$.

The third L1495 core, shown in Fig. 1-5, is L1495B, and lies $\sim 8'$ west of L1495A–S. This core is weaker and smaller than the other L1495 cores. In contrast with those cores, L1495B has few

significantly asymmetric CS spectra. The symmetric δV_{CS} distribution (Fig. 6-d), the mean δV_{CS} value of 0.04 \pm 0.13, and high P from the t-test (Table 2 and 3) are consistent with no evidence for inward motions in this core.

L1521F – Observations of this source show that features of the spectral asymmetry can be dependent on the observing tracer or the observing spatial resolution. L1521F has been classified as an infall candidate by LMT99 based on their high angular resolution CS(2-1) observations, and by Onishi et al. (1999) from their $HCO^+(3-2)$ & (4-3) data (note that these authors named this core as MC27). Our map, however, indicates an extended red asymmetry over the core (Fig. 1-6). Further study of this object in different tracers is needed to clarify its kinematics.

TMC2– The N_2H^+ emission of this core is extended (about $6' \times 6'$) both N-S and E-W (Fig. 1-7). Most CS spectra show skewed blue asymmetry, and the Gaussian fit velocities of N_2H^+ lie on the skewed red part or the red shoulder of the CS spectra, suggesting possible extended inward motions. The infall radius of this core is somewhat large (0.13 \sim 0.14 pc) and the infall speed is the largest in our sample (\sim 0.17 km s⁻¹), making the mass infall rate also the largest one (4.0 \times 10⁻⁵ M_{\odot} yr⁻¹).

TMC1– TMC1 has been the best target in Taurus for an extensive study of the physics of star formation and the chemistry (e.g., Hirahara et al. 1992, Langer et al. 1995, and Pratap et al. 1997). It is known to be very extended, about 12' by over 35' in C¹⁸O (2 – 1) (Langer et al. 1995). Our map shows only a part around the center of TMC1. The distribution of N₂H⁺ is extended NW - SE (Fig. 1-8). Some CS spectra show blue-skewed asymmetric shapes, while others are closer to Gaussian. However, the Gaussian fit velocities of the N₂H⁺ spectra are located somewhere toward the red of the CS spectra, regardless of the CS line shape. Moreover, careful inspection of the average CS spectrum on the right panel in Fig. 1-8 indicates that TMC1 may have one or two different velocity components shown as two wings to each side of the strong peak component. A two-layer model fit to the strong peak component gives a possible infall speed of $\sim 0.05 \text{ km s}^{-1}$. The estimated infall radius is at least $\sim 0.16 \text{ pc}$, and the mass infall rate is about $0.6 \times 10^{-5} \text{ M}_{\odot} \text{ yr}^{-1}$.

L1512– The distribution of N_2H^+ emission from this core is rather compact and round. The line width of this source is the narrowest ($<\Delta V_{N_2H^+}>\approx 0.19~{\rm km~s^{-1}}$) among our sources. The HCO⁺ (3 – 2) spectrum which Gregersen & Evans (2000) have obtained toward this source shows no asymmetric feature. This may be partially because the spectral resolution (0.12 – 0.15 km⁻¹) that they used was not sufficient to resolve it. On the other hand, our observation shows clear asymmetric features in spectra which are also changing over the core. As in L1495A–N, the sense of the asymmetry in the CS spectra changes from blue to red with respect to an SW – NW axis (indicated with solid line in Fig. 1-9), again suggesting differential rotation.

L1622A– This core has two N₂H⁺ condensations forming a NE-SW filament (Fig. 1-12). We refer to the weaker NE condensation as **L1622A-1**, and to the brighter SW condensation as **L1622A-2**. Both condensations have similar systemic V_{LSR} ($\approx 0.2 - 0.3 \text{ km s}^{-1}$), but their

 δV_{CS} distributions are different, as L1622A-2 has more blue asymmetric CS spectra (Fig. 6-b) than L1622A-1 (Fig. 6-e). Because of its blue asymmetric spectra, L1622A-2 is selected as a probable infall candidate. The estimated infall radius, speed, and mass infall rate for this core are 0.24 - 0.26 pc, ~ 0.09 km s⁻¹, and 1.2×10^{-5} M_{\odot} yr⁻¹, respectively.

L183– This core is one of the largest in our sample, and mapping its total extent required covering an area of $\sim 11' \times 18'$. As Fig. 1-13 shows, the N₂H⁺ emission lies mostly along the N-S direction. In the BM89 catalog, the brightest position was referred to as L183B and the weaker position as L183. Here, we treat the system as a single core (L183) because there is no clear boundary between the peaks in the N₂H⁺ emission.

The spatial distribution of self-absorbed CS spectra is rather complicated as described in §3.4. The number distribution of δV_{CS} of all spectra of this source is rather close to symmetric. However, this source was classified as a strong infall candidate because the inner region (within the HM) of the N₂H⁺ core shows high blue excess and a significantly asymmetric δV_{CS} distribution to the blue, while the outer region does not (Fig. 1-13 and Fig. 6). A more detailed study is needed to understand the kinematics of L183.

L1689B− L1689B is known to be a small core (FWHM mass of $\sim 0.6 M_{\odot}$) located at the east edge of L1689 complex of Ophiuchus star forming region (Loren 1989, André et al. 1996). Our N₂H⁺ map shows a structure with a very compact center and a diffuse envelope elongated NW − SE (Fig. 1-14).

Several molecular line observations toward this core [CS (2-1); LMT99, H₂CO $(2_{12}-1_{11}$; Bacmann et al. 2000, HCO⁺ (3-2); Gregersen & Evans 2000] have revealed a typical infall asymmetry in their spectra. It has been suggested that this core is just entering the phase of dynamical contraction following the formation of a super-critical core, as revealed from 1.3mm continuum, and ISOCAM absorption studies by André et al. (1996) and Bacmann et al. (2000).

Our spectral line observations strongly support the above suggestion. The CS spectra present extended infall asymmetry, in the form of double peaks, blue peak with a red shoulder, and blue-skewed peaks, implying extended inward motions over the source. The infall radius, speed, and mass infall rate are 0.08 - 0.18 pc, ~ 0.05 km s⁻¹, and $\sim 0.5 \times 10^{-5}$ M_{\odot} yr⁻¹, respectively.

L234E- This region has three well defined N₂H⁺ cores: **L234E-N, C,** and **S** (Fig. 1-16). **L234E-S**, the most southern one, has the largest negative $\langle \delta V_{CS} \rangle$ (-0.63 ± 0.14), a blue asymmetric δV_{CS} distribution, and a low P value (≈ 0), which make it a strong infall candidate. Most CS spectra present double peaks or a blue peak with a red shoulder. We estimate the core infall radius, speed, and mass infall rate are 0.06 - 0.12 pc, 0.05 km s⁻¹, and $0.4 - 0.6 \times 10^{-5}$ M_{\odot} yr⁻¹, respectively.

L234E-C also show infall asymmetry at some positions, but not as many as L234E-S. This source has one position with $\delta V_{CS} \leq -5 \sigma_{\delta V_{CS}}$, so its infall radius is estimated from one half the telescope FWHM, corresponding to 0.02 pc. The infall speed and mass infall rate are estimated in

 $0.05~{\rm km~s^{-1}}~{\rm and} \sim 0.33 \times 10^{-5}~{\rm M_{\odot}~yr^{-1}}.$

L234E–N has no position with $\delta V_{CS} \leq -5 \sigma_{\delta V_{CS}}$, although its δV_{CS} distribution is skewed to the blue. We classify this as a member of Group 4.

L429-1– The N_2H^+ peak emission in this core lies to the NW of the CS emission (Fig. 1-18), some $\sim 88''$ away from the map center position which was defined by the optical minimum in the Digitized Sky Survey image (LM99). Most CS profiles show a very strong self-absorption feature with brighter red peak, as found in L1521F.

L694-2− This is one of our strong infall candidates. The CS profile map shows double peaked infall profiles near the N_2H^+ peak region, which change to blue-skewed and symmetric at larger separation (Fig. 1-19). The distance to L694-2 is not yet known, although we assume it is the same as that to B335 (250 pc), because L694-2 lies within a few degrees of B335 and has similar LSR velocity. Infall radius, speed, and mass infall rate are 0.09 - 0.13 pc, 0.05 - 0.07 km s⁻¹, and $0.4 - 0.6 \times 10^{-5}$ M_☉ yr⁻¹, respectively.

L1155C- L1155C is a dense molecular condensation within a dark cloud L1158 in Cepheus. Harjunpää et al. (1991) have observed this source in CO, ¹³CO, C¹⁸O, HCO⁺, and NH₃, and have found two cores with slightly different velocities. These authors suggest that the cores might be a bound pair. From a test of Jeans instability, one core (L1155C-2) has been suggested to be probably collapsing. Note that we we have named the bright core as L1155C-1, and the weak one as L1155C-2, following LMT99. Harjunpää et al., however, have referred to them in the opposite way.

Our observations (Fig. 1-20) also shows two distinct cores with slightly different systemic velocities, L1155C-1 ($V_{LSR} \approx 2.7 \text{ km s}^{-1}$) and L1155C-2 ($V_{LSR} \approx 1.4 \text{ km s}^{-1}$).

The CS spectra on the right panels in Fig. 1-21 and 22 show additional velocity components superposed along the line of sight. Both cores show a significant number of infall profiles, and are classified as strong infall candidates. Their δV_{CS} distributions shown in Fig. 6-a clearly indicate overabundance of blue asymmetric CS spectra (both double peaks and single peaks with infall asymmetry). L1155C-2 is elongated N-S and twice as large as L1155C-1 (Fig. 1-21). It has a large velocity gradient along the major axis ($\sim 0.19~\rm km~s^{-1}~arcmin^{-1}$), which can confuse the interpretation of the simple average CS spectrum. For this reason, we present in the right panel of Fig. 1-21 the spectra averaged within the HM contour of the N₂H⁺ emission after coinciding the systemic velocities of the spectra with that at peak position [($\Delta \alpha, \Delta \delta$) = (-88'', -132'')]. The estimated infall radius is the largest in our sample ($0.12 - 0.45~\rm pc$), and the infall speeds and mass infall rates are $0.07 - 0.10~\rm km~s^{-1}$ and $0.4 - 1.2 \times 10^{-5}~\rm M_{\odot}~yr^{-1}$, respectively. L1155C-1 is located NE of L1155C-2 and has a smaller, more compact N₂H⁺ distribution (Fig. 1-22). There is no significant velocity gradient, so the profiles shown in Fig. 1-22 are averages over the HM contour of the N₂H⁺ emission. The infall radius, speed, and mass infall rate for this core are $0.15 - 0.25~\rm pc, 0.09 - 0.1~\rm km~s^{-1}$, and $2.3 \sim 2.5 \times 10^{-5}~\rm M_{\odot}~yr^{-1}$, respectively.

4 SUMMARY 19

4. Summary

We have carried out an extensive mapping survey of starless cores in optically thick [CS(2-1)] and thin $[N_2H^+ (1-0)]$ and $C^{18}O (1-0)$ lines searching for infall candidates and studying the general features of inward motions in the earliest stage of star formation. The FCRAO 14-m telescope equipped with the focal plane receiver array systems QUARRY and SEQUOIA was used for these observations. Fifty out of 52 cores were detected in CS(2-1), 34 out of 45 were detected in $N_2H^+ (1-0)$, and 28 out of 29 were detected in $C^{18}O (1-0)$. A total of 33 regions with strong emission have been mapped in both CS and N_2H^+ , identifying 37 well-defined N_2H^+ starless cores. The N_2H^+ emission is usually very compact and shows a well defined peak, while the CS and $C^{18}O$ emissions are much more diffuse. CS spectra in a large number of starless cores show profiles with infall asymmetry, while most of the N_2H^+ spectra show a single Gaussian profile in their isolated component. The typical sizes and line widths (FWHM) of the N_2H^+ cores are found to be between ~ 0.05 pc and ~ 0.13 pc, and 0.2-0.4 km s⁻¹, respectively.

We have quantified the kinematical properties of each core by using the normalized velocity difference δV_{CS} between the thick CS and thin N₂H⁺ peak velocities. We have also defined δV_{CS} -related parameters, such as the blue excess E and the t-test probability value P. Using these parameters and the shapes of the CS lines, we have classified the starless cores into five distinctive groups:

- (1) cores with "very significant blue excess" having overabundance of blue asymmetric CS spectra with *double* peaks—L1498, L1495A—S, L1544, L1689B, L234E-S, L492, L694-2, L1155C-2, and L1155C-1, and possibly L183.
- (2) cores with "significant blue excess" having overabundance of blue asymmetric CS spectra with a *single* peak–L1355, TMC2, TMC1, L1552, L1622A-2, L158, and L234E-C, and possibly L981-1 and L1197.

We propose that these cores in groups 1 and 2 are bona fide infall candidates.

- (3) cores with "significant red excess" having overabundance of red asymmetric CS spectra–L1521F, L429-1, and CB246.
- (4) cores with "no significant excess" having small spread in δV_{CS} L1333, L1495B, L1400A, L1517B, L1622A–1, L234E-N, and L1696A.
- (5) cores with "no significant excess" having large spread in δV_{CS} L1495A–N, L1507A, and L1512.

Using our spectroscopic data we determine the main properties of our nineteen infall candidates: infall radii, speeds, and mass rates. We estimate infall radii from the δV_{CS} distribution and from the distribution of blue-skewed CS spectra, finding values typically between 0.06 and 0.14 pc.

The infall speed for each core is derived by fitting the spectra with a simple two layer radiative transfer model, and typical values are between 0.05 and 0.09 km s⁻¹. Finally, approximate mass infall rates are found to range from a few 10^{-6} to 10^{-5} M_{\odot} yr⁻¹. As these infall speeds were obtained using line-of-sight velocities, real (3D) values of the infall speed and the mass infall rate should be larger than our estimates by a factor of 1–2.

A comparison of the equivalent radius of the N_2H^+ core with the infall radius shows that larger cores tend to have larger infall radii by a factor of about 2-3, suggesting that the infall motions are likely involved in the process of core condensation.

The parameters of the infall kinematics found in the starless cores of our sample are very similar to those seen in L1544. The infall speed and the extent of the infall zone found in our study can be explained with models of ambipolar diffusion in super-critical or slightly sub-critical cores, or with models of turbulence dissipation, although further work is needed for a more detailed comparison. Our observations suggest that extended inward motions with large speed are fairly common in starless cores, and that such inward motions may be a necessary step in the condensation of a star-forming dense core.

We thank Tyler Bourke and Jonathan Williams for help during the observations, and Carl Gottlieb for communicating his new frequency measurements prior to publication. We also thank an anonymous referee for helping us to improve this paper. C.W.L. acknowledges the financial support by 1996 Overseas Postdoctoral Support Program of Korea Research Foundation and partial support by "Spectroscopic Observational Study of Celestial Object with Optical and Radio Telescopes" 99-NQ-01-01-A of the Korea Astronomy Observatory. C.W.L. also thanks the Harvard-Smithsonian Center for Astrophysics for support while working on this project. M.T. acknowledges partial support from Spanish DGES grant PB96-104. This research was supported by NASA Origins of Solar System Program, Grant NAGW-3401.

A. Selection and Effects of the New Line Frequencies

As LMT99 pointed out, in a quantitative study of the infall profiles of starless cores with narrow lines, the uncertainty in the laboratory determinations of the line frequencies can be a critical issue. Here we describe the frequency set we have adopted for this study, and how this choice affects our previous results in LMT99.

In LMT99, we chose a frequency set based on the comparison of different line profiles in the starless core L1544 (Tafalla et al. 1998), and in this way, assumed frequencies of 97980.950 MHz for CS (2–1) and 93176.265 MHz for the "isolated" component ($F_1F = 01 - 12$) of N_2H^+ (1 – 0). This values were at the time more accurate than the existing laboratory determinations, and were probably limited by the non Gaussian shape of the line profiles in L1544. Since then, a set of more accurate laboratory measurements (Gottlieb 2000, private communication) has yielded the

following frequencies: $97980.953(\pm 0.002)$ MHz for CS (2–1) and $109782.173(\pm 0.002)$ MHz for C¹⁸O (1 – 0), although unfortunately no N₂H⁺ measurement with equivalent accuracy has been obtained yet.

The new laboratory measurement of CS (2–1) agrees within the errors with the choice in LMT99, so its effect on the LMT99 CS velocities is minor. Given the critical need for our work of an equivalently accurate N_2H^+ determination, we have carried out new astronomical observations of L1512 (the core with narrowest lines) using the IRAM 30m telescope (Tafalla et al. 2001, in preparation). We have observed simultaneously $C^{18}O$ (1 – 0) and N_2H^+ , and used the new laboratory $C^{18}O$ (1 – 0) frequency to determine a value of 93176.258 MHz for the $F_1F = 01 - 12$ component of N_2H^+ (1 – 0). A comparison of the two spectra (assuming the new frequencies) is shown in Fig. 11.

The new CS(2–1) and N_2H^+ (1 – 0) frequencies are slightly different from those in LMT99 (3 and 7 kHz, respectively), and their use decreases the velocity shift between the two profiles by about 0.013 km s⁻¹. The effect of this change on the δV_{CS} distribution is to make it less skewed to the blue. In Fig. 12 we show how the frequency choice affects the δV_{CS} distribution in the sample of starless cores studied by LMT99. Cases (a) and (b) are the same as shown in Fig. 6 of LMT99, except for a different binning in case (a). In other words, case (a) uses Lovas (1992) frequency (97980.968 MHz) for CS (2–1) and 93176.265 MHz for N_2H^+ "isolated" component by Caselli et al. (1995), and case (b) uses 97980.950 MHz for CS and 93176.265 MHz for N_2H^+ , as preferred by LMT99. Case (c) shows the δV_{CS} distribution with the present 'best' frequency set (97980.953 MHz for CS and 93176.258 MHz for N_2H^+). As it can be seen, the new and more accurate set of frequencies still makes the δV_{CS} histogram significantly skewed to the blue, so the main conclusion in LMT99, that inward motions are a significant feature of starless cores, is still valid. In addition, the new frequency set does not change the list of 7 strong and 10 probable infall candidates suggested by LMT99.

REFERENCES

Adelson, L.M. & Leung, C.M. 1988, MNRAS, 235, 349

André, P., Ward-Thompson, D., & Motte, F. 1996, A&A, 314, 625

Bacmann, A., André, P., Pujet, J.-L., Abergel, A., Bontemps, S., & Ward-Thompson, D. 2000, A&A, 361, 555

Benson P.J., & Myers P.C. 1989, ApJS, 71, 89 (BM89)

Buisson, G., Desbats, L., Duvert, G., Forveille, T., Gras, R., Guilloteau, S., Lucas, R., & Valiron, P. 1994, CLASS Manual (Grenoble: IRAM)

Ciolek, G.E., & Basu, S. 2000, ApJ, 529, 925

Ciolek, G.E., & Mouschovias, T.Ch. 1995, ApJ, 454, 194

Caselli, P., Myers, P.C., & Thaddeus, P. 1995, ApJ, 455, L77

Gregersen, E.M., Evans, N. J., Zhou, S., & Choi, M. 1997, ApJ, 484, 256

Gregersen, E.M., & Evans, N. J. 2000, ApJ, 538, 260

Harjunpää, P., Liljeström, T., & Mattila, K. 1991, 249, 493

Hirahara et al. 1992, ApJ, 394, 539

Indebetouw, R., & Zweibel, E.G. 2000, ApJ, 532, 361

Jijina, J., Myers, P.C., & Adams, F.C. 1999, ApJS, 125, 161

Kuiper, T.B.H., Langer, W.D., & Velusamy, T. 1996, 468, 761

Lee, C. W., & Myers, P.C. 1999, ApJS, 123, 233 (LM99)

Lee, C. W., Myers, P.C., & Tafalla, M. 1999, ApJ, 526, 788 (LMT99)

Langer, W.D., Velusamy, T., Kuiper, B.H., Levin, S., Olsen, E., & Migenes, V. 1995, ApJ, 453, 293

Leung, C.M., & Brown, R.B. 1977, ApJ, 214, L73

Lemme, C., Walmsley, C.M., Wilson, T.L., & Muders, D. 1995, A&A, 302, 509

Li, Z. 1999, ApJ, 526, 806

Loren, R.B. 1989, ApJ, 338, 902

Lynds, B. T. 1962, ApJS, 7, 1

Mardones, D., Myers, P.C., Tafalla, M., Wilner, D.J., Bachiller, R., & Garay, G. 1997, ApJ, 489, 71

Myers, P.C., Fuller, G.A., Goodman, A.A., & Benson, P.J. 1991, ApJ,376, 561

Myers, P.C., Mardones, D., Tafalla, M., Williams, J.P., & Wilner, D.J. 1996, ApJ, 465, 133

Myers, P.C., & Lazarian, A. 1998, ApJ, 507, L157

Myers, P.C., & Zweibel, E.G. 2001, ApJ, submitted.

Nakano, T. 1998, ApJ, 494, 587

Pratap, P., Dickens, R.L., Snell, M.P., Miralles, E.A., Bergin, E.A., Irvine, W.M., & Schloerb, F.P. 1997, ApJ, 486, 862

Onishi, T., Mizuno, A., & Fukui, Y. 1999, PASJ, 51, 257

Shu, F.H. 1977, ApJ, 214, 488

Shu, F.H., Adams, F.C., & Lizano, S. 1987, ARAA, 25, 23

Tafalla, M., Mardones, D., Myers, P.C., Caselli, P., Bachiller, R., & Benson, P.J. 1998, ApJ, 504, 900 (T98)

Williams, J.P., Myers, P.C., Wilner, D.J., & Di Francesco, J. 1999, ApJ, 513, L61

Wolkovitch, D., Langer, W.D., Goldsmith, P.F., & Heyer, M. 1997, ApJ, 477, 241

Zhou, S. 1995, ApJ, 442, 685

Zhou, S., Evans, N.J., Kömpe, C., & Walmsley, C.M. 1993, ApJ, 404, 232

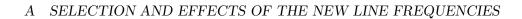
Zweibel, E.G. 1998, ApJ, 499, 746

This preprint was prepared with the AAS IATEX macros v4.0.

FIGURE CAPTIONS

- Fig. 1. Selected CS and N₂H⁺ emission maps of starless cores. Most figures consist of a CS profile map superposed on a N₂H⁺ integrated intensity map on the left panel, and of average CS and N₂H⁺ spectra over the half maximum contour of the N₂H⁺ intensity map on the right panel. The dashed lines on the profiles indicate the N₂H⁺ peak velocities. For some large sources with multiple cores such as L1495 (Fig. 1-4) and L1155C (Fig. 1-20), we present maps of the overall distribution of N₂H⁺ integrated intensity. L1155C-2 (Fig. 1-21) has a large velocity gradient across the core ($\sim 0.19 \text{ km s}^{-1} \text{ arcmin}^{-1}$), so simply averaging the spectra will hide any possible infall feature. Thus, for this core we have shifted the systemic velocity of the spectra to make them coincide with that at the brightest N_2H^+ position $(\Delta\alpha, \Delta\delta) = (-88'', -132'')$, and then we have averaged all spectra within the HM contour of the N₂H⁺ emission. The solid lines crossing cores L1495A-N (Fig. 1-5) and L1512 (Fig. 1-9) indicate the possible rotation axis of these cores (see §3.9 for further details). Lowest, half maximum, and peak levels of the N₂H⁺ integrated intensity $(\int T_A^* dv)$ for each core are as follows (in K km s⁻¹); (1) L1333 - 0.108, 0.540, 1.080, (2) L1355 -0.051, 0.256, 0.512, (3) L1498 - 0.100, 0.500, 1.000, (4) L1495, (5) L1495A-N - 0.150, 0.750, 1.500;L1495A-S - 0.078, 0.390, 0.078, (6) L1521F - 0.13, 0.883, 1.766, (7) TMC2 - 0.163, 0.816, 1.631, 0.816, 0.81(8) TMC1 - 0.249, 1.245, 2.490, (9) L1512 - 0.093, 0.463, 0.926 (10) L1544 - 0.2, 1.452, 2.904, (11) L1552 - 0.100, 0.689, 1.377, (12) L1622A-1 - 0.096, 0.479, 0.957; L1622A-2 - 0.100, 0.927, 1.853,(13) L183 - 0.160, 0.799, 1.598, (14) L1689B - 0.064, 0.322, 0.643, (15) L158 - 0.055, 0.274, 0.548, (16) L234E-N - 0.088, 0.442, 0.883; L234E-C - 0.067, 0.332, 0.672; L234E-S - 0.094, 0.470, 0.940, (17) L492 - 0.142, 0.711, 1.421, (18) L429-1 - 0.178, 0.891, 1.782, (19) L694-2 - 0.167, 0.835, 1.670, (20) L1155C, (21) L1155C-2 - 0.070, 0.348, 0.695, (22) L1155C-1 - 0.075, 0.374, 0.748, (23) L981-1 - 0.075, 0.374, 0.748, (23) L981-1 - 0.075, 0.374, 0.748, (24) L981-1 - 0.075, 0.374, 0.748, (25) L981-1 - 0.075, 0.374, 0.748, (26) L981-1 - 0.075, 0.374, 0.748, (27) L981-1 - 0.075, 0.374, 0.748, (28) L981-1 - 0.075, 0.075, 0.075, 0.075, 0.075, 0.075, 0.075, 0.075, 0.075, 0.075, 0.075, 0.075, 0.075, 0.075, 0.075, 0.075, 0.0-0.045, 0.225, 0.449, (24) L1197 - 0.073, 0.365, 0.729,
- Fig. 2. N_2H^+ line width versus size for the N_2H^+ cores in our sample. The core size is the equivalent radius of the half maximum (HM) contour of the N_2H^+ integrated map, and the line width is the average of the FWHMs of the line profiles whose peak S/N is better than 5. Filled squares, triangles, and open circles represent strong infall candidates, possible infall candidates, and all of non-infall candidates, respectively, which we classify in §3-4. In the figure we exclude six cores (CB23, L1689B, L429–1, L1148B, L981–1, and L1063) because of the large uncertainty in their $<\Delta V_{N_2H^+}>(\sigma_{<\Delta V_{N_2H^+}>}\gtrsim 0.03~{\rm km~s^{-1}})$.
- Fig. 3. Number distributions of $\langle \delta V_{CS} \rangle$ for our sample of starless cores. This histogram shows that most of our sources have a global overabundance of blue spectra characteristic of inward motions. Note, however, that this does not necessarily reflect a statistical excess of infall motions in starless cores, because many sources in our present sample have been selected with a bias toward infall candidates found in previous observations. For L183, we use a $\langle \delta V_{CS} \rangle$ from the spectra within the HM contour of the N₂H⁺ emission.

- **Fig. 4.** Mean of δV_{CS} ($<\delta V_{CS}>$) versus blue excess (E) for each source. Note the good correlation. The error bar of δV_{CS} is 1 standard error of the mean $<\delta V_{CS}>$. For L183, we use spectra within the HM contour of the N₂H⁺ map (see text).
- Fig. 5. Mean of δV_{CS} ($<\delta V_{CS}>$) versus probability of the t-test (P). Note how P approaches zero as $<\delta V_{CS}>$ deviates from zero. The error bar is 1 standard error of the mean $<\delta V_{CS}>$. For L183, we use only spectra within the HM contour of the N₂H⁺ map (see text).
- Fig. 6. Number distributions of δV_{CS} for cores in our five groups; (a) group 1 cores with "very significant blue excess" having overwhelming overabundance of blue asymmetric CS spectra with double peaks "strong infall candidates", (b) group 2 cores having similar spectral properties as those in the group 1, and having single-peaked CS spectra which are skewed to the blue blue "probable infall candidates", (c) group 3 cores with "significant red excess" having overwhelming overabundance of red asymmetric CS spectra, (d) group 4 cores with "no significant excess" having a small spread in δV_{CS} , and (e) cores with "no significant excess" having a large spread in δV_{CS} . All histograms are normalized by the total number of samples. For L183, we use only spectra within the HM contour of the N₂H⁺ map (see text).
- Fig. 7. Number distributions of infall radii for (a) weak, (b) strong cases determined from the δV_{CS} distribution, and (c) case determined from the distribution of blue-skewed CS profiles. See text in §3.5 for a more detailed explanation of the three cases.
- Fig. 8. Best fit results of a two-layer radiative transfer model to observed spectra. Model spectra (thick solid line) are superposed on the observed spectra (thin histogram). W and S mean the 'weak' and 'strong' cases, respectively, as described in $\S 3.6$. Each observed spectrum is an average of spectra satisfying each case, except for the S case in L1155C-2, where the spectrum at (-88'', -176'') is presented. For the S case in L234E-S, one spectrum (out of 3) was discarded because its systemic velocity is slightly different from that of the other spectra.
- Fig. 9. Number distribution of infall speeds for (a) 'weak' and (b) 'strong' cases
- Fig. 10. Comparison of the infall radius with the size of the N_2H^+ emission. Three cases are presented: (a) weak case, (b) strong case from the δV_{CS} distribution, and (c) case determined from the distribution of blue-skewed CS profiles. L183 has not been included because this core is assumed to be a strong infall candidate from a statistics of the spectra within the HM contour of the N_2H^+ map, so its infall radius was simply assumed to be equal to the equivalent radius of the HM contour.
- **Fig. 11.** Comparison of $C^{18}O$ (1-0) and N_2H^+ (1-0) $F_1F = 01-12$ toward L1512, the core with the narrowest lines. For $C^{18}O$ (1-0), we have used the the recent laboratory determination by C.Gottlieb (priv. comm.): $109782.173(\pm 0.002)$ MHz. For N_2H^+ (1-0) $F_1F = 01-12$, we have derived a frequency of 93176.258 MHz from the best match with $C^{18}O$ (1-0).



26

Fig. 12. — Effect of the choice of frequencies for CS (2–1) and N_2H^+ (1 – 0) on the distribution of δV_{CS} in starless cores (LMT99 data). Fig. 1-(a) and (b) are the same as Fig. 6 of LMT99, and Fig. 1-(c) shows the result of using our new set of frequencies. Note how the new frequencies make the δV_{CS} histogram still significantly skewed to the blue.

arXiv:astro-ph/0105515v1 30 May 2001

 ${\rm TABLE~1}$ Starless core regions mapped in CS (2 - 1), N_2H^+ (1 - 0), and $C^{18}O$ (1 - 0). a

Source	RA 1950 h m s	DEC 1950	Array	CS	N_2H^+	$\mathrm{C}^{18}\mathrm{O}$	selection basis
L1333	02 21 10.1	75 13 31	S	D	D		3
L1355	$02\ 48\ 41.4$	$68\ 43\ 36$	S(Q)	D	D		1
L1498	$04\ 07\ 50.0$	$25\ 02\ 13$	S(Q)	D	D	D	1
L1495	$04\ 15\ 25.5$	$28\ 19\ 31$	S(Q)	D	D		5
L1521B	$04\ 21\ 08.5$	$26\ 30\ 00$	Q	D	ND	D	4
L1521F	$04\ 25\ 35.0$	$26\ 45\ 00$	S(Q)	D	D		1
L1400FD	$04\ 25\ 52.6$	$54\ 05\ 47$	Q	D	ND	D	5
L1521E	$04\ 26\ 17.0$	$26\ 07\ 47$	Q	D	ND	D	4
L1400A	$04\ 26\ 50.6$	$54\ 46\ 08$	S(Q)	D	D	D	3
L1445	$04\ 28\ 28.8$	$46\ 31\ 01$	S	D	ND	D	2
TMC2	$04\ 29\ 46.9$	$24\ 18\ 54$	S(Q)	D	D	D	2
ON32	$04\ 36\ 24.0$	$25\ 45\ 00$	Q	D	D		5
TMC1	$04\ 38\ 29.0$	$25\ 39\ 01$	S(Q)	D	D		4
ON34	$04\ 38\ 42.0$	$25\ 36\ 00$	S(Q)	D	D		5
L1507A	$04\ 39\ 29.0$	$29\ 38\ 07$	Q	D	D		3
CB23	$04\ 40\ 22.0$	$29\ 34\ 26$	Q	D	D		2
L1517C	$04\ 51\ 35.9$	30 30 00	Q	D	ND	D	4
L1517A	$04\ 51\ 54.8$	$30\ 28\ 53$	Q	D	D	D	3
L1517B	$04\ 52\ 07.2$	30 33 18	Q	D	D	D	3
L1512	$05\ 00\ 54.4$	$32\ 39\ 00$	S(Q)	D	D	D	3
L1544	$05\ 01\ 14.0$	$25\ 07\ 00$	S(Q)	D	D		2
L1552	$05\ 14\ 34.9$	$26\ 02\ 07$	S(Q)	D	D		3
L1622	$05\ 52\ 02.9$	$01\ 53\ 15$	S(Q)	D	D		2
L134A	$15\ 50\ 58.1$	-04 26 36	Q	D	D	D	3
L183	$15\ 51\ 30.0$	-02 42 51	S(Q)	D	D	D	1
L1696A	$16\ 25\ 29.9$	-24 12 32	$\hat{\mathbf{Q}}$	D	D	D	3
L1696B	$16\ 26\ 01.5$	-24 14 59	Q	D	D	D	2
L1709A	$16\ 27\ 50.0$	-23 34 37	Q	D	ND	D	3
L1709C	$16\ 30\ 52.5$	-23 32 18	Q	D		D	4
L1689B	$16\ 31\ 43.6$	-24 31 40	S(Q)	D	D	D	2
L158	$16\ 44\ 37.7$	-13 54 03	S	D	D		1
L191	$16\ 44\ 41.5$	-12 23 20	Q	D	ND	D	4
L204C	$16\ 44\ 51.0$	-12 02 47	Q	D		D	4
L204B	$16\ 45\ 00.0$	-11 50 00	Q	D		D	4
L204F	$16\ 45\ 01.3$	-11 51 40	Q	D	ND	D	4
L234E	$16\ 45\ 22.6$	-10 52 10	S	D	D		2
L63	$16\ 47\ 21.0$	-18 01 00	Q	D		D	3
L492	18 13 11.6	-03 47 17	\mathbf{S}	D	D		2
L429-1	$18\ 14\ 28.2$	-08 14 40	\mathbf{S}	D	D		3
L694-2	$19\ 38\ 42.4$	$10\ 49\ 59$	\mathbf{S}	D	D		1
L1155C	$20\ 43\ 00.0$	$67\ 41\ 47$	S(Q)	D	D	D	1
L1147	$20\ 40\ 00.0$	$67\ 11\ 00$	$\hat{\mathbf{Q}}$	D	ND	D	4
L1148	$20\ 40\ 38.8$	$67\ 09\ 48$	S		D		3
L1082C	$20\ 50\ 19.6$	$60\ 07\ 15$	Q	D			4
L981-1	$20\ 58\ 36.3$	50 08 19	$_{ m S}$	D	D		3
L1063	$21\ 06\ 44.6$	$56\ 06\ 09$	\mathbf{S}	D	D		3
L1235B	$22\ 14\ 41.2$	$73\ 07\ 31$	Q	D		D	5

TABLE 1—Continued

Source	RA 1950 h m s	DEC 1950	Array	CS	$\mathrm{N_2H^+}$	$\mathrm{C^{18}O}$	selection basis
L1235	22 14 41.4	73 09 25	Q	D	ND		4
L1197	$22\ 35\ 08.1$	$58\ 41\ 45$	\mathbf{S}	D	D		3
L1103	$22\ 40\ 14.3$	$56\ 27\ 58$	Q	ND	ND	ND	5
L1234	$23\ 16\ 08.4$	$62\ 12\ 08$	Q	ND			3
CB244	$23\ 25\ 00.5$	$74\ 01\ 06$	Q	D		D	5
CB246	$23\ 54\ 12.0$	$58\ 17\ 47$	Q(S)	D	D	D	3

a The first column indicates the name of the observed region, and the second and third columns list the central coordinates in B1950 epoch. The 4th column designates the receiver array, QUARRY (Q) and SEQUOIA (S), and 'S(Q)' means that both SEQUOIA and QUARRY observations were carried out. 'D', 'ND', and ' ⋯ ' in the 5th to 7th columns indicate 'Detection', 'No Detection', and 'Not Observed', respectively. The last column indicates the selection criterion for each source: 1 & 2 − selected as strong or probable infall candidate according to LMT99, 3 − selected from strong CS & N_2H^+ detection according to LMT99, 4 − selected from NH₃ detection according to BM89, and 5 − selected from LM99 catalog.

 ${\rm TABLE~2}$ Starless ${\rm N_2H^+~Cores},~{\rm and~Their~Velocity~and~Map~Information.}^a$

Source	RA 1950	DEC 1950	$\left(\frac{A}{\pi}\right)^{1/2}$	< V _{CS} >	$< V_{N_2H^+} >$	$<\Delta V_{N_2H^+}>$	N	R	$<\delta V_{CS}>$	$<\tau_{N_2H^+}>$
	n m s	0 / //	(pc)	$(km s^{-1})$	(km s^{-1})	(km s^{-1})		(pc)		
L1333	02 21 10.1	75 13 31	(0.76')	3.84 ± 0.06	3.86 ± 0.05	0.34 ± 0.02	5	(1.20')	-0.07±0.05	1.0±0.1
L1355	$02\ 48\ 41.4$	68 43 36	Ò.05	-3.89 ± 0.02	-3.77 ± 0.02	0.25 ± 0.03	4	ò.05	-0.48 ± 0.07	0.2 ± 0.1
L1498	$04\ 07\ 50.0$	$25\ 02\ 13$	0.05	7.69 ± 0.01	7.81 ± 0.01	0.20 ± 0.01	15	0.08	-0.66 ± 0.04	0.7 ± 0.1
L1495B	$04\ 14\ 59.0$	$28\ 15\ 05$	0.04	6.57 ± 0.02	6.55 ± 0.04	0.37 ± 0.03	3	0.03	0.04 ± 0.13	0.5 ± 0.2
L1495A-N	$04\ 15\ 25.5$	28 20 15	0.05	7.36 ± 0.05	7.30 ± 0.01	0.33 ± 0.01	18	0.11	0.25 ± 0.15	0.5 ± 0.1
L1495A-S	$04\ 15\ 35.6$	28 16 35	0.06	7.19 ± 0.02	7.31 ± 0.01	0.26 ± 0.01	14	0.14	-0.45 ± 0.09	$0.8 {\pm} 0.2$
L1521F	$04\ 25\ 35.0$	$26\ 45\ 00$	0.04	6.62 ± 0.01	6.48 ± 0.01	0.27 ± 0.01	10	0.07	0.53 ± 0.04	1.0 ± 0.1
L1400A	$04\ 26\ 55.7$	$54\ 46\ 08$	0.06	3.22 ± 0.03	3.20 ± 0.03	0.25 ± 0.01	12	0.10	0.10 ± 0.05	$0.6 {\pm} 0.2$
TMC2	$04\ 29\ 46.9$	$24\ 18\ 54$	0.06	6.05 ± 0.01	6.13 ± 0.02	0.33 ± 0.01	40	0.13	-0.24 ± 0.03	0.6 ± 0.1
TMC1	$04\ 38\ 29.0$	$25 \ 39 \ 01$	0.05	5.72 ± 0.02	5.89 ± 0.01	0.32 ± 0.01	28	0.15	-0.52 ± 0.05	0.5 ± 0.1
L1507A	$04\ 39\ 29.0$	$29\ 38\ 07$	0.04	6.14 ± 0.04	6.18 ± 0.01	0.22 ± 0.01	3	0.05	-0.17 ± 0.20	0.2 ± 0.1
CB23	$04\ 40\ 18.2$	29 33 36	0.03	6.04 ± 0.02	6.02 ± 0.02	0.22 ± 0.03	0		0.14 ± 0.17	
L1517B	$04\ 52\ 07.2$	30 33 18	0.04	5.82 ± 0.02	5.81 ± 0.01	0.21 ± 0.02	4	0.04	0.04 ± 0.07	0.9 ± 0.2
L1512	$05\ 00\ 50.9$	32 39 00	0.04	7.02 ± 0.04	7.06 ± 0.02	0.19 ± 0.01	10	0.07	-0.22 ± 0.16	0.4 ± 0.1
L1544	$05\ 01\ 10.8$	$25\ 07\ 00$	0.03	7.08 ± 0.08	7.14 ± 0.02	0.28 ± 0.02	5	0.05	-0.24 ± 0.26	$0.8 {\pm} 0.2$
L1552	$05\ 14\ 31.6$	$25\ 02\ 07$	0.03	7.60 ± 0.01	7.69 ± 0.01	0.21 ± 0.00	7	0.06	-0.46 ± 0.03	1.0 ± 0.2
L1622A-2	$05\ 52\ 02.9$	$01 \ 53 \ 15$	0.11	1.03 ± 0.02	1.09 ± 0.01	0.28 ± 0.01	10	0.27	-0.22 ± 0.06	0.7 ± 0.2
L1622A-1	$05\ 52\ 17.5$	$01\ 56\ 56$	0.15	1.18 ± 0.02	1.15 ± 0.03	0.25 ± 0.01	10	0.25	0.13 ± 0.07	0.5 ± 0.1
L134A	$15\ 50\ 54.8$	-04 26 36	0.05	2.76 ± 0.01	2.72 ± 0.04	0.23 ± 0.01	2	0.08	0.16 ± 0.21	
L183	$15\ 51\ 29.9$	-02 43 35	0.11	2.34 ± 0.02	2.37 ± 0.01	0.26 ± 0.01	55	0.28	-0.06 ± 0.07	0.7 ± 0.1
				2.32 ± 0.02	2.40 ± 0.01	0.25 ± 0.01	20		-0.32 ± 0.09	0.9 ± 0.1
L1696A	$16\ 25\ 29.9$	-24 12 32	0.04	3.42 ± 0.02	3.39 ± 0.03	0.21 ± 0.01	3	0.04	0.15 ± 0.16	0.3 ± 0.2
L1689B	16 31 43.6	-24 31 40	0.04	3.44 ± 0.04	3.54 ± 0.02	0.32 ± 0.03	8	0.09	-0.30 ± 0.11	0.2 ± 0.1
L158	$16\ 44\ 33.7$	-13 53 19	0.04	3.79 ± 0.03	3.91 ± 0.01	0.21 ± 0.01	6	0.07	-0.60 ± 0.09	0.3 ± 0.1
L234E-N	$16\ 45\ 16.2$	-10 41 53	0.05	2.88 ± 0.02	2.92 ± 0.02	0.19 ± 0.01	8	0.08	-0.16 ± 0.07	0.8 ± 0.2
L234E-C	$16\ 45\ 16.1$	-10 44 05	0.03	2.88 ± 0.06	2.92 ± 0.01	0.22 ± 0.01	3	0.04	-0.18 ± 0.20	0.1 ± 0.1
L234E-S	$16\ 45\ 22.6$	-10 52 10	0.04	2.89 ± 0.03	3.05 ± 0.02	0.26 ± 0.01	6	0.06	-0.63 ± 0.14	0.6 ± 0.2
L492	$18\ 13\ 07.9$	-03 47 16	0.04	7.63 ± 0.05	7.74 ± 0.01	0.31 ± 0.02	7	0.09	-0.35 ± 0.21	1.0 ± 0.3
L429-1	$18\ 14\ 22.2$	-08 14 39	0.05	7.01 ± 0.07	6.82 ± 0.02	0.42 ± 0.03	12	0.11	0.47 ± 0.16	0.4 ± 0.1
L694-2	$19\ 38\ 42.4$	$10\ 49\ 59$	0.04	9.41 ± 0.01	9.59 ± 0.02	0.25 ± 0.01	7	0.09	-0.73 ± 0.08	0.7 ± 0.2
L1155C-2	$20\ 42\ 28.6$	$67\ 37\ 25$	0.15	1.30 ± 0.06	1.44 ± 0.06	0.30 ± 0.02	12	0.31	-0.51 ± 0.05	0.5 ± 0.1
L1155C-1	20 43 00.0	$67\ 41\ 47$	0.13	2.54 ± 0.01	2.70 ± 0.02	0.38 ± 0.02	6	0.15	-0.45 ± 0.04	0.4 ± 0.2
L1148A*	$20\ 40\ 38.8$	$67\ 09\ 48$	0.06		2.59 ± 0.01	0.24 ± 0.02	4	0.08		0.2 ± 0.1
L1148B*	$20\ 40\ 31.4$	$67\ 12\ 00$	0.04		2.58 ± 0.03	0.28 ± 0.06	1	0.04		
L981-1	$20\ 58\ 36.4$	50 09 03	0.12	-0.20 ± 0.01	-0.06 ± 0.01	0.36 ± 0.04	1	0.09	-0.41 ± 0.07	0.6 ± 0.3
L1063	$21\ 06\ 44.6$	$56\ 06\ 09$	0.13	-0.94 ± 0.02	-0.86 ± 0.02	0.36 ± 0.05	1	0.10	-0.23 ± 0.09	1.2 ± 0.6
L1197	$22\ 35\ 08.1$	$58\ 41\ 45$	0.06	-3.20 ± 0.03	-3.12 ± 0.02	0.23 ± 0.00	3	0.10	-0.37 ± 0.04	0.5 ± 0.1
CB246	$23\ 54\ 17.5$	$58\ 17\ 47$	0.04	-0.76 ± 0.03	-0.83 ± 0.01	0.28 ± 0.01	7	0.05	0.28 ± 0.09	0.5 ± 0.1

a This table lists the thirty seven N₂H⁺ cores for which the spatial extent and the strongest positions are well defined. L1148A and B have no δV_{CS} information because they were observed in N₂H⁺ (1 − 0) only. The first column indicates the name of the N₂H⁺ core, and the second and the third columns list the coordinates in B1950 epoch of the positions of N₂H⁺ peak intensity, which are sometimes slightly different from those of the map centers given in Table 1. Column 4 lists an equivalent radius $(A/\pi)^{1/2}$ of the N₂H⁺ emission, where A is an area inside the half maximum contour of N₂H⁺ integrated emission. The velocities and their $<\delta V_{CS}>$ given in columns 5 to 7 and column 10 are averages of Gaussian fit velocities and δV_{CS} of the spectra whose peak S/N ratio is better than 5: $<V_{CS}>=\sum_i V_{CS}^i/N$, $<V_{N_2H^+}>=\sum_i V_{N_2H^+}^i/N$, $<\Delta V_{N_2H^+}>=\sum_i \Delta V_{N_2H^+}^i/N$, and $<\delta V_{CS}>=\sum_i \delta V_{CS}^i/N$, where $\delta V_{CS}=(V_{CS}-V_{N_2H^+})/\Delta V_{N_2H^+}$. CB23 has no δV_{CS} spectra detected with S/N better than 5, so the values for this source are averages from spectra with marginal detection. All estimates are given with the standard error of the mean (s.e.m). N in column 8 is the number of samples for which the peak S/N of the spectra is larger than 5. 'R' in column 9 is one half the largest separation between positions having spectra with peak S/N larger than 5. The core distances used to derive linear radii are mainly from Lee & Myers (1999) and references therein. We assume that the distance to L694-2 is the same as to B335 (250 pc) because L694-2 lies within a few degrees of B335 and has a similar LSR velocity. The distance to the L1197 was taken as 400 pc following Jijina, Myers, & Adams (1999). The spatial extent for L1333 is given in angular scale due to unknown distance. < $\tau_{N_2H^+}$ in column 11 is the optical depth of the isolated (F₁F = 01 − 12) hyperfine component in a core map, defined as one-ninth of the total optical depth of the 1 − 0

 ${\rm TABLE~3}$ δV_{CS} related parameters of Starless ${\rm N_2H^+~Cores.^a}$

Source	N_{-}	N_{+}	N_0	N	Е	Р
L1333	0	0	11	12	0.00	0.30
L1355	5	0	7	12	0.42	0.00
L1498	14	0	6	20	0.70	0.00
L1495B	0	1	6	7	-0.14	0.80
L1495A-N	11	11	7	29	0.00	0.17
L1495A-S	11	0	15	26	0.42	0.00
L1521F	0	10	4	14	-0.71	0.00
L1400A	0	0	24	24	0.00	0.02
TMC2	25	0	24	49	0.51	0.00
TMC1	26	0	16	42	0.62	0.00
L1507A	0	0	9	9	0.00	0.08
CB23	0	0	4	4	0.00	0.47
L1517B	0	0	7	7	0.00	0.93
L1512	4	3	7	14	0.07	0.12
L1544	7	1	9	17	0.35	0.00
L1552	7	0	6	13	0.54	0.00
L1622A-2	5	2	10	17	0.18	0.08
L1622A-1	0	2	10	13	-0.15	0.82
L134A	0	0	9	9	0.00	0.00
L183	15(13)	3(1)	52(6)	76(20)	0.12(20)	0.62(0.00)
L1696A	Ó	Ó	` ′ 7	7	$\stackrel{\circ}{0}.0\stackrel{\circ}{0}$	$0.3\overset{'}{5}$
L1689B	7	2	5	14	0.36	0.01
L158	2	0	11	13	0.15	0.00
L234E-N	0	0	11	11	0.00	0.01
L234E-C	1	0	7	8	0.13	0.01
L234E-S	4	0	6	10	0.40	0.00
L492	5	1	2	8	0.50	0.10
L429-1	4	9	3	16	-0.31	0.02
L694-2	8	1	3	12	0.58	0.01
L1155C-2	9	0	9	18	0.50	0.00
L1155C-1	4	0	5	9	0.44	0.00
L1148A						
L1148B						
L981-1	2	0	1	3	0.67	0.08
L1063	0	0	1	1	0.00	
L1197	1	0	3	$\overline{4}$	0.25	0.05
CB246	0	$\overline{2}$	9	11	-0.18	0.03

^a N₋ is the number of positions with $\delta V_{\rm CS} \leq -5~\sigma_{\delta V_{\rm CS}},~N_+$ the number of positions with $\delta V_{\rm CS} \geq 5~\sigma_{\delta V_{\rm CS}},~N_0$ the number of positions with $-5~\sigma_{\delta V_{\rm CS}} < \delta V_{\rm CS} < 5~\sigma_{\delta V_{\rm CS}},~{\rm and}~N=N_-+N_++N_0.$ E in column 6 is the 'blue excess,' defined as E = $(N_--N_+)/N$. 'P' in the last column is the probability of drawing the observed δV_{CS} distribution from a zero mean t-distribution, calculated from a student t-test. For L183, we give two measurements using all spectra in the N_2H^+ core (given without parenthesis) and using only spectra within the HM contour of the N_2H^+ emission (bracketed with parenthesis).

TABLE 4 Results of Line Profile Model for 19 Starless Cores. $^{\rm a}$

Source	Case	$ au_0$	σ (km s ⁻¹)	Т _г (К)	$V_{\rm thin} \ ({\rm km~s}^{-1})$	$V_{\rm in,z} \ ({\rm km\ s}^{-1})$	$ m R_{in}(\delta V_{CS}) \ (pc)$	R _{in} (CS) (pc)	$(\times 10^4 cm^{-3})$	$\stackrel{\dot{\mathrm{M}}}{(\times 10^{-5}\mathrm{M}_{\odot}\;year^{-1})}$
L1355	W	0.68	0.14	7.9	-3.75	0.121	0.11	0.20	0.91	0.84
L1498	W	1.53	0.09	7.0	7.79	0.044	0.08	0.08	0.71	0.13
	S	1.55	0.09	7.8	7.78	0.030	0.05		1.82	0.09
L1495A-S	W	1.33	0.20	5.1	7.36	0.078	0.09	0.12	2.78	1.11
	S	1.33	0.20	5.1	7.36	0.072	0.09		2.78	1.03
TMC2	W	1.04	0.26	7.8	6.40	0.165	0.13	0.14	2.25	3.97
TMC1	W	0.60	0.18	12.2	5.77	0.052	0.17	0.16	0.63	0.60
L1544	W(S)	3.26	0.11	9.2	7.19	0.021	0.07	0.09	1.39	0.09
L1552	Ŵ	1.60	0.14	7.1	7.78	0.116	0.07	0.12	2.25	0.81
L1622A-2	W	1.18	0.19	9.0	1.21	0.093	0.23	0.24	0.30	1.20
L183	S	1.27	0.24	6.3	2.57	0.048	0.11		2.68	0.98
L1689B	W	1.56	0.17	10.1	3.60	0.050	0.08	0.18	2.54	0.51
	S	1.57	0.17	10.1	3.97	0.048	0.08		2.54	0.49
L158	W	1.46	0.17	5.0	3.98	0.074	0.02	0.11	40.61	0.76
L234E-C	W	0.97	0.14	9.2	2.89	0.047	0.02	0.07	27.54	0.33
L234E-S	W	0.98	0.17	10.9	3.03	0.054	0.06	0.12	4.51	0.56
	S	1.22	0.15	12.1	3.06	0.050	0.06		3.51	0.40
L492	W	0.78	0.21	8.8	7.72	0.086	0.07	0.09	5.06	1.35
	S	1.38	0.17	7.9	7.70	0.043	0.05		6.50	0.44
L694-2	W	1.73	0.16	5.9	9.63	0.074	0.12	0.13	1.00	0.67
	S	2.08	0.16	6.2	9.64	0.054	0.09		1.78	0.49
L1155C-2	W	1.19	0.18	6.1	1.24	0.100	0.22	0.45	0.38	1.15
	S	1.69	0.13	6.0	1.62	0.065	0.12		0.66	0.39
L1155C-1	W	1.47	0.27	5.7	2.87	0.096	0.12	0.25	2.85	2.49
	S	1.50	0.27	5.6	2.86	0.089	0.09		5.06	2.31
L981-1	W(S)	0.90	0.18	5.3	-0.04	0.098	0.19	0.31	0.50	1.13
L1197	W	1.45	0.11	8.0	-3.11	0.050	0.05	0.10	2.72	0.22

^a This table presents infall parameters for 19 infall candidates. The first column indicates the name of the N_2H^+ core. In the second column, 'W' means the 'weak' case considering all blue asymmetric spectra satisfying $\delta V_{\rm CS} \le -5 \, \sigma_{\delta V_{\rm CS}}$, 'S' means the 'strong' case considering only those CS spectra with double-peaked infall asymmetry satisfying $\delta V_{\rm CS} \le -5 \, \sigma_{\delta V_{\rm CS}}$, and 'W(S)' means that the W and S cases produce the same average spectrum. If no 'S' is listed, there are no double-peaked spectra having S/N > 5. The τ₀ (the peak optical depth) in the 3rd column, the σ (the velocity dispersion) in the 4th column, the T_r (the excitation temperature of the rear layer) in the 5th column, the V_{thin} (the peak velocity of the optically thin spectrum) in the 6th column, and the V_{in,z} (one dimensional infall speed of the gas layers) in the 7th column are obtained from the best least squares fit of the two layer radiative transfer model to the observed spectrum. We give two infall radii in the 8th and 9th columns of which R_{in}(δV_{CS}) is determined from δV_{CS} distribution, and R_{in}(CS) is determined from the spatial extent of the blue-skewed CS profiles The gas (H₂) density in the 10th column is the density of a core in virial equilibrium with radius (R_{in}) and velocity dispersion (σ) which approximates the density associated with the gas causing the absorption dip or shoulder. The last column lists the mass infall rates of the cores. For L183, all parameters are from the fit of the average spectrum over the N₂H⁺ HM contour. As most spectra within the N₂H⁺ HM contour satisfy the 'strong' case condition, we regard the L183 fit as representing the 'strong' case.